ON THE BEHAVIOR OF NONLINEAR HYDRODYNAMIC COEFFICIENTS OF A SUBMERGED CYLINDER BENEATH THE WATER SURFACE

Nguyen Van My[1], Le Anh Tien[1], Phan Hoang Nam[1,*], Nguyen Quoc Khanh[1], Chau Van Than[1], Phan Thanh Hoang[2]

[1]*The University of Danang - University of Science and Technology, Da Nang, Vietnam*
[2]*School of Mechanical Engineering, Pusan National University, Busan 46241, Republic of Korea*
[*]E-mail: phnam@dut.udn.vn

Abstract. This study aims at numerically exploring the behavior of flow fields and nonlinear hydrodynamic coefficients of a horizontal cylinder beneath the free surface flow considering the effects of nonlinear surface waves and various cylinder shapes. The computational model is based on two-dimensional incompressible Navier–Stokes solvers along with the treatment of the free surface flow using the volume of fluid method. The effect of the turbulent flow is also considered by using the shear stress transport turbulence model. The simulation result of a benchmark case study of the submerged cylinder is first validated with available experiment data, where a mesh convergence analysis is also performed. Afterward, the flow fields and hydrodynamic force coefficients around the cylinder surface are analyzed, and the influences of various cylinder shapes and Reynolds numbers on the hydrodynamic coefficients are investigated. A state diagram representing the hydrodynamic behavior including stable and unstable stages is finally proposed; this is an important criterion for the practice design of submerged civil structures under the free surface flow.

Keywords: submerged cylinder, free surface flow, two-phase mixture model, nonlinear hydrodynamic coefficient, VOF method.

1. INTRODUCTION

Partially or fully submerged bodies beneath the free surface flow have been found in many structural engineering problems, e.g., piles [1], sea walls, breakwaters [2,3], bridge piers, abutment [4], or decks [5,6] under the wave or flood impacts. Due to the complex nonlinear wave of the free surface, the interaction between the structure partially or fully submerged beneath the wave surface and the flow is rather complicated than that of a deeply submerged body [7]. Concerning these phenomena, researchers have paid more attention to dynamic impact forces caused by wave and flood flows in hazard conditions.

Free surface flows over a submerged body are costly to achieve by experiments, which require numerous experiment facilities; therefore, an alternative is the use of computational fluid dynamic solvers to explore in detail the flow characteristic. In the literature, there have been studies focusing on both experimental and numerical models for hydrodynamic pressure characteristics of a submerged body with simple shapes. Malavasi and Guadagnini [8] performed laboratory-scale experiments to investigate the interaction between the free-surface flow and a cylinder of rectangular cross-section, considering various flow conditions and elevations of the cylinder above the channel floor. The authors provided mechanism insights of local velocities around the cylinder structure and hydrodynamic force frequencies. Bai et al. [9] experimentally and numerically studied interaction mechanisms of a horizontal cylinder near the free surface with considering wave-current forces. The authors found that the force amplitude increases due to wave reflections and decreases due to wave blockages. Chu et al. [10] experimentally investigated the interaction between the free-surface flow and a smooth, submerged circular cylinder. Flume experiments were performed to measure the surface pressure and water surface depth. The influences of the Froude number, blockage ratio, gap ratio, and depth ratio on the flow field and force coefficients of the cylinder were also estimated. The force coefficient relations under these above-considered parameters were explored and could be used in the structural design of submerged pipelines. Recently, Ren et al. [11] estimated the hydrodynamic loads on partially submerged cylinders at a high Re number (i.e., $Re = 9 \times 10^5$). The authors explored that free surface effects result to a significant mean downward lift force in the crossflow direction.

The numerical simulation approach for investigating the impact force on submerged bodies has also been a great concern. This approach offers the ability to predict in detail velocity, pressure, and flow field distributions, which can allow detailed studies on the physical mechanism of the flow. Reichl et al. [12] numerically investigated the two-dimensional (2D) flow past a cylinder close to the free surface at low Reynolds number conditions. Surface vorticity mechanisms under different Froude numbers were explored. Besides, the authors presented a mechanism of the wake state switching generation which is controlled by a feedback loop. Bozkaya and Kocabiyik [13] studied the free surface wave interaction with an oscillating cylinder by solving unsteady Navier-Stokes equations. The author observed two new locked-on states of vortex formation in the near wake region. Kara et al. [14] presented a detailed numerical simulation of the flow over a submerged bridge using the large eddy simulation (LES) method, and the level set method was applied to capture the complex water surface profiles. The obtained LES results revealed the complex nature of the flow featuring various vortical features around the body. Liu et al. [15] performed 2D simulations to investigate characteristics of the flow past a plate normal to a stream, where a multiphase flow model coupled with the volume of fluid (VOF) method, and the k–ω shear stress transport turbulence model was also adopted. The effects of the plate depth were mainly examined, and the authors concluded that the drag coefficient can be reduced up to 38% when the plate is closer to the surface. In addition, a jet mechanism was also observed in the shallow submerged case. Zhong et al. [16] conducted numerical predictions of the hydrodynamic properties of a rectangular cylinder close to the free surface. The effects of the depth-to-length ratio

were considered. The authors concluded that the free surface effects on the flow past rectangular cylinders are more significant when the depth-to-length ratio is lower than 1.0. Attiya et al. [17] simulated multiphase flows past a submerged plate in the proximity of the free surface at a high Reynolds number of 50,000. Details of the Karman vortex shedding from the top surface of the plate were observed, and the force coefficient distribution under different length ratios was investigated. The authors observed that the lift coefficient is the highest for the length ratio of 2.5.

As a successor of the above numerical studies, this paper pays more attention to the nonlinear hydrodynamic forces and their behavior on a submerged cylinder beneath the water surface (i.e., the depth-to-length ratio < 1.0 as observed by Zhong et al. [16]). In particular, a reliable coupling model of the Navier–Stokes solver and the free surface treatment able to accurately predict the free surface flow field is first presented and validated. The effect of the free surface to flow field characteristics and the influences of various cylinder shape ratios and Reynolds numbers on the behavior of the hydrodynamic forces are then comprehensively evaluated. As a result, optimal relations between the shape ratio and the Reynolds number are finally presented in terms of the stability of the hydrodynamic force acting on the cylinder. The finding from the study is a significant contribution to the practical design of the bridge deck, pier, or any structures with a rectangular section submerged under the free surface flow.

2. NUMERICAL SIMULATION MODEL

2.1. Two-phase mixture model with the free surface treatment

To deal with the two-phase water-air flow, a Reynolds-averaged homogeneous mixture model is adopted [18]. Both phases are assumed as immiscible, incompressible fluids, and share the same pressure and velocity fields. The two phases are distinguished by the gas or water volume of fraction. Due to the assumed isothermal modeling for the considered problem, the energy equation can be ignored. Thus, the basic form of the Reynolds-average equations for two-phase flows includes the mixture continuity equation and the mixture momentum equations and could be written as

$$\frac{\partial u_j}{\partial x_j} = 0, \tag{1}$$

$$\frac{\partial u_i}{\partial t} + u_j \frac{\partial u_i}{\partial x_j} = -\frac{1}{\rho_m}\frac{\partial p}{\partial x_i} + g_i + \mu_m \frac{\partial^2 u_i}{\partial x_j} - \frac{\partial \overline{u_i' u_j'}}{\partial x_j}, \tag{2}$$

where the subscripts $i, j = 1, 2, 3$ denote $x, y,$ and z directions, respectively; $p, u,$ and u' are the pressure, flow mean velocity, and the fluctuating velocities in 2D or 3D directions, respectively; t is the physical calculation time; g is the gravitational acceleration term; ρ_m is the mixture density; and μ_m is the mixture viscosity.

The values of mixture density and mixture viscosity are determined via the volume of fraction of each continuity phase, given as

$$\rho_m = \sum_{s=1}^{2} \alpha_s \rho_s = \alpha_w \rho_w + \alpha_g \rho_g, \tag{3}$$

$$\mu_m = \sum_{s=1}^{2} \alpha_s \mu_s = \alpha_w \mu_w + \alpha_g \mu_g, \tag{4}$$

where α_w and α_g are the volume of fraction of the water and gas, respectively; ρ_w, μ_w and ρ_g, μ_g are the density, viscosity of the water and gas, respectively.

As mentioned above, the Reynolds-averaged Navier–Stokes (RANS) equations are adopted for the multiphase flow modeling. A turbulence model needs to be included to predict the fluctuating velocity components $(\overline{u_i' u_j'})$ to close the governing equations. The fluctuating terms are linearly modeled to the mean velocity, given as

$$-\overline{u_i' u_j'} = \mu_t \left(\frac{\partial u_i}{\partial x_j} + \frac{\partial u_j}{\partial x_i} \right) - \frac{2}{3} k \delta_{ij}. \tag{5}$$

The shear stress transport k–ω model introduces the conservation equations of the turbulent kinetic energy k and the turbulent frequency ω, given as

$$\frac{\partial k}{\partial t} + u_j \frac{\partial k}{\partial x_j} = \frac{\partial}{\partial x_j} \left(\left(\nu + \frac{\nu_t}{\tilde{\sigma}_k} \right) \frac{\partial k}{\partial x_j} \right) + \frac{1}{\sigma} \tilde{P}_k - \beta^* k \omega, \tag{6}$$

$$\frac{\partial \omega}{\partial t} + u_j \frac{\partial \omega}{\partial x_j} = \frac{\partial}{\partial x_j} \left(\left(\nu + \frac{\nu_t}{\tilde{\sigma}_\omega} \right) \frac{\partial \omega}{\partial x_j} \right) + \tilde{C}_\alpha \frac{\omega}{k} \nu_t \left(\frac{\partial u_i}{\partial x_j} + \frac{\partial u_j}{\partial x_i} \right) \frac{\partial u_i}{\partial x_j} - \tilde{C}_\beta \omega^2 + 2 \left(1 - F_1 \right) \sigma_{\omega 2} \frac{\partial k}{\partial x_j} \frac{\partial \omega}{\partial x_j}. \tag{7}$$

where β^*, $\tilde{C}_\alpha$, $\tilde{C}_\beta$, $\sigma_{\omega 2}$ are closure constant coefficients; F_1 is a coupling function; and $\tilde{P}_k$ is the production of the turbulent kinetic energy and is determined as

$$\tilde{P}_k = \min \left(\rho \nu_t \left(\frac{\partial u_i}{\partial x_j} + \frac{\partial u_j}{\partial x_i} \right) \frac{\partial u_i}{\partial x_j}, 10 \beta^* \rho k \omega \right), \tag{8}$$

with $\nu_t = \dfrac{k}{\omega}$ and the turbulent eddy viscosity (μ_t) is determined as

$$\mu_t = \frac{0.31 k}{\max \left(0.31 \omega, \sqrt{2} S_t F_2 \right)}, \tag{9}$$

where S_t is the magnitude of the strain rate and F_2 is a function that is one for the boundary-layer flow and zero for the free shear layer.

The homogeneous mixture model usually results in largely diffuse interfaces, which cannot accurately capture the physical insight for multiphase flow predictions, especially for the hydrodynamic force problem. To maintain the interface sharpness and achieve good conservation of mass, the VOF method [19–21] is used extensively for solving the large moving interface deformations.

The phasic gas volume fraction equation is written as

$$\frac{\partial \alpha_g}{\partial t} + \frac{\partial \left(\alpha_g u_j \right)}{\partial x_j} = 0. \tag{10}$$

In the VOF method, the indicator function α_g represents the phasic volume fraction of the gas phase. The value of α_g equal 1.0 presents for pure gas phase, while α_g equal

0.0 presents for pure water phase. The interfaces between the two-phase are presented by the values ranging by $0.0 < \alpha_g < 1.0$.

2.2. Numerical solution

The governing equation system is discretized by the finite volume method on the computational structure grid domain. The pressure-based solver with the SIMPLE (i.e., semi-implicit method for pressure-linked equations) procedure is applied to solve the equation. The physical time derivative term is approximated by applying the first-order implicit scheme. For spatial discretization, the least-squares cell-based method is adopted. The convective and viscous terms in the momentum equation are treated by using the first-order upwind scheme. Concerning the VOF model, the implicit compressive scheme is adopted to obtain high accuracy in the large interface deformation. The numerical method is implemented using the ANSYS FLUENT scheme programming [22], which allows a flexible input for different cases.

3. NUMERICAL RESULTS AND DISCUSSIONS

3.1. Numerical model validation

To demonstrate the accuracy of the numerical model, the simulation of the free surface flow over a benchmark case of the submerged cylinder is performed and compared with experimental data conducted by Chu et al. [10]. In the experiment, the water flow with the presence of the free surface over a smooth circular cylinder was studied in a rectangular cross-section channel. The cylinder with a diameter of $D = 0.02$ m and a width of $L = 0.12$ m was located inside the channel. Surface pressures on the cylinder were measured by pressure transducers and the free surface shape was also captured in the experiment.

At first, a planar 2D computational domain is adopted for the 2D numerical simulation, as shown in Fig. 1. To reduce the outlet condition effect, an extension of the downstream with $20D$ is adopted while the upstream region is $10D$. Two important quantities that mainly affect the hydrodynamic forces of the submerged body are the water depth (h) and the gap between the channel bed and the cylinder (S). The ratios of $h/D = 0.8$ and $S/D = 1.5$ are used, which are identical to that of the experimental study. A depth-averaged uniform velocity of $U = 0.395$ m/s, corresponding to a Reynolds number of 7,900, is estimated. Regarding the boundary conditions, the constant velocity is adopted at the inlet domain, while the zero gradient pressure is applied at the outlet condition. The channel bed and cylinder are modeled by the no-slip wall condition, and the top domain is applied as the open condition where the atmospheric pressure is maintained.

A mesh solution considering more clustering near the cylinder wall and free surface is adopted to accurately capture the hydrodynamic forces and free surface motion. The detail of the mesh distribution around the cylinder is shown in Fig. 2. To consistently obtain numerical predictions, grid and time step independent studies are first performed; three grids with different resolutions are adopted as given in Table 1. The first internal grid points are located in the viscous sublayer and logarithmic area where the time-averaged $y+$ around the surface of the cylinder is about 1.1 for all considered grids.
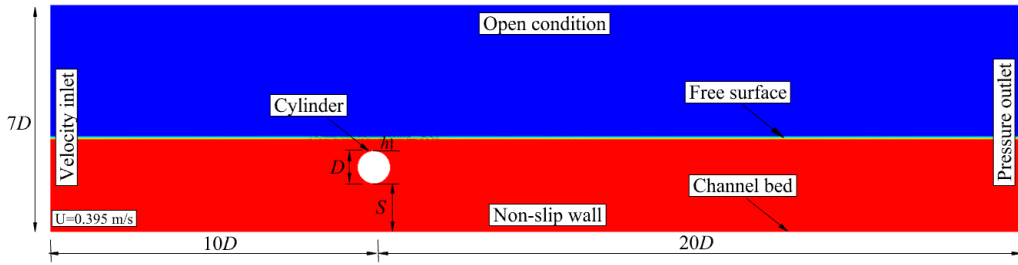
Fig. 1. Computational domain of the benchmark case and applied boundary conditions
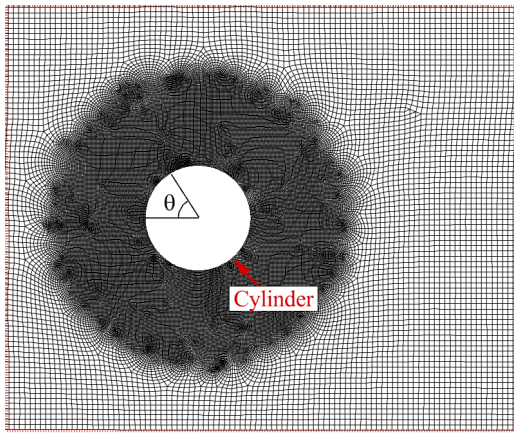

Fig. 2. An example of the mesh distribution around the cylinder in the case of fine grid
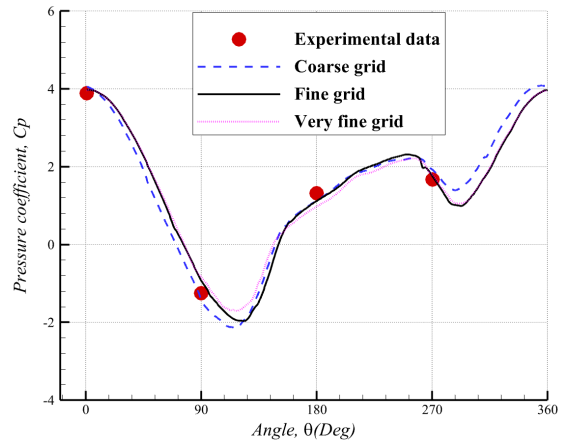

Fig. 3. Surface pressure coefficient under different grid resolutions

Table 1. Parameters for three different grid resolutions

Grid name	Total number of nodes	Grid node on the cylinder surface (k)
Coarse grid	88,665	189
Fine grid	112,649	267
Very fine grid	162,499	399

The predicted time-averaged cylinder surface pressure coefficients C_p using the considered grid resolutions are compared in Fig. 3. In which, the general equation for the calculation of C_p in the case of steady or unsteady flow over a body is obtained as

$$C_p = \frac{1}{N} \sum_{i=1}^{N} \frac{p_i - p_\infty}{\frac{1}{2}\rho U^2},\tag{11}$$

where p_i is the pressure on the cylinder surface for specific grid node i (with N is the number of grid nodes on the surface), p_∞ denotes the reference pressure, $p_\infty = 101{,}325$ Pa,

ρ denotes the water density, ρ = 998 kg/m^3, and U is the uniform velocity at the inlet condition.

The hydrodynamic force coefficients including the drag C_D, lift C_L, and moment C_M forces are determined from the surface pressure on the cylinder as

$$C_D = \frac{F_D}{0.5\rho U^2 A}, \quad C_L = \frac{F_L - B}{0.5\rho U^2 A}, \quad C_M = \frac{M}{0.5\rho U^2 AR}. \tag{12}$$

The forces are calculated as

$$F_D = \sum_{i=1}^{N} P\left(\varnothing_i\right)\cos\left(\varnothing_i\right)\left(LR\Delta\varnothing\right),$$

$$F_L = -\sum_{i=1}^{N} P\left(\varnothing_i\right)\sin\left(\varnothing_i\right)\left(LR\Delta\varnothing\right), \tag{13}$$

$$M = \sum_{i=1}^{N} P\left(\varnothing_i\right)\cos\left(\varnothing_i\right)\left(LR\Delta\varnothing\right)d_i,$$

where $A = L2R$ is the projected area of the cylinder; L and R are the width and radius of the cylinder, respectively; $B = \rho g\pi\left(2R\right)^2 L/4$ is the buoyancy of the cylinder; $\varnothing_i$ the angle between the horizontal and a line of force; $\Delta\varnothing$ is the angle between two adjacent lines of force; and d_i is the perpendicular distance from the line of action of the force to the pivot.

As shown in Fig. 3, a similar pattern is observed for the three cases of the grid resolution; however, careful readers can see a gap of C_p exhibited at the cylinder surface locations from 90 to 290 degrees. It can be seen that with the presence of the free surface, lower values of C_p on the top cylinder are captured. In general, the trend of the surface pressure coefficient is similar to the measured data in the experiment. Besides, the predicted drag force under coarse, fine, and very fine grids are 1.93, 2.08, and 2.09, respectively. In comparison with the previous study by Chu et al. [10] using a large-eddy simulation model, i.e., C_D = 2.1–2.2, an agreement within 6% is obtained. To evaluate the influence of the time step values on the predicted

Fig. 4. Time-step refinement testing for surface pressure coefficient C_p

numerical results, four different time step sizes, i.e., dt = 0.001 (s), 0.002 (s), 0.01 (s), and 0.02 (s), are considered. The numerical simulations are performed on the fine grid which was obtained from the previous grid convergence study. Fig. 4 shows the comparison of the predicted surface pressure coefficient under different time step numbers. The predicted results are almost similar, and a larger time step size results in a divergence solution is found for this problem. Following the above analyses, the numerical
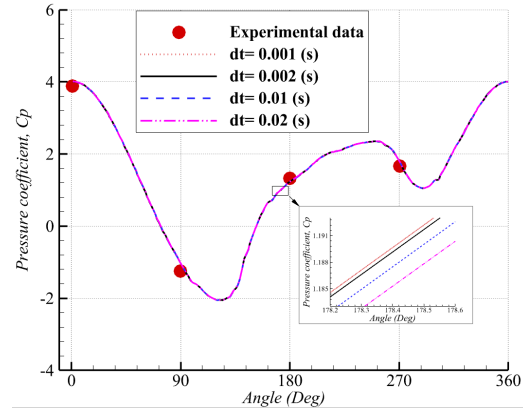
results are grid and time step independent, and the fine grid with a time step of 0.002 (s) is employed for the subsequent computations.

Fig. 5 presents a comparison of the free surface shape between the numerical prediction and experimental observation at the steady stage. As a result of the VOF simulation, the free surfaces are captured by the water volume fraction ranging from 0.0 to 1.0. Due to the blockage effect, the water depth at the upstream section is increased and a smooth reduction of free surface depth around the cylinder is observed. At the downward section, the simulated free surface is undisturbed, and a flat shape is obtained far from the cylinder. In comparison with measured experimental data, the free surface shapes are well reproduced by the present numerical simulation.
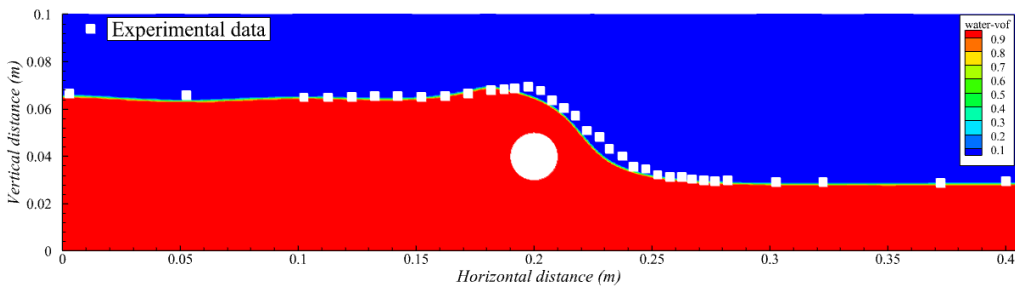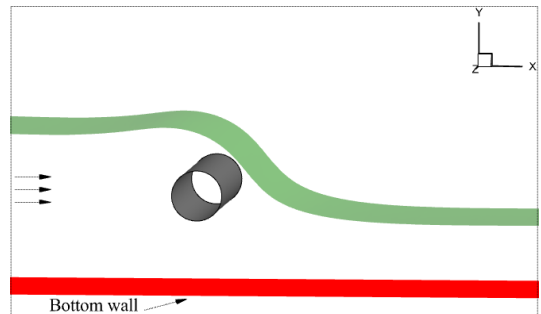

Fig. 5. Comparison of free surface position at the steady stage
with experimental data by Chu et al. [10]

(a) Experimental snapshot

(b) 3D numerical simulation

Fig. 6. Comparison of the free surface shape between the numerical simulation and available experiment at the steady stage

Following the 2D simulation, a three-dimensional simulation (3D) considering the effects of the span-wise direction of the above validation case is also performed to get closer to real flow fields. The free surface profile is captured in Fig. 6 with the snapshot from the experiment. As observed that the free surface keeps smooth in the span-wise direction and there is no obvious difference between the 2D and 3D models. By considering the time computational efficiency, the 2D model with the fine grid is adopted for the

next simulations. In summary, the numerical simulation is reliable for investigating the nonlinear hydrodynamic forces acting on a horizontal cylinder beneath the water surface.

3.2. Flow field characteristics

Fig. 7(a) presents instantaneous velocity fields with streamlines around the cylinder at the steady stage. The free surface line is formed on the elements with a water volume fraction of 50%. Due to the small gap ratio h/D, the cylinder blocks the flow passing through the gap under the free surface, resulting in a remarkable reduction of the water depth in the downward section; and thus, causing the increase of the flow velocity, as shown in Fig. 7(a).
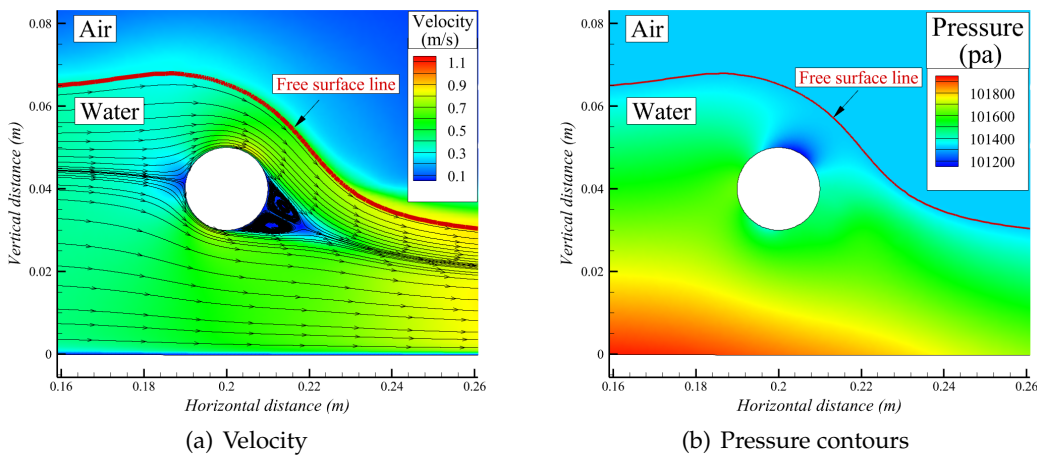

(a) Velocity　　　　　　　　　(b) Pressure contours

Fig. 7. Flow fields around the circular cylinder with the free surface

An important mechanism of the flow is the occurrence of the wake flow behind the cylinder, which mainly induces a periodic variation of the hydrodynamic forces. Because of the inclination of the free surface, cylinder wake vortices are formed with the inclined downward direction; this causes the increase of the hydrodynamic forces due to the increase of the drag, lift, and moment as compared with that in the unbounded flow condition. The pressure distribution around the cylinder is also shown in Fig. 7(b). In the presence of the free surface, an inclined low pressure at the top cylinder region is observed. Thus, the cylinder is mainly subjected to upward lift and downward drag forces.
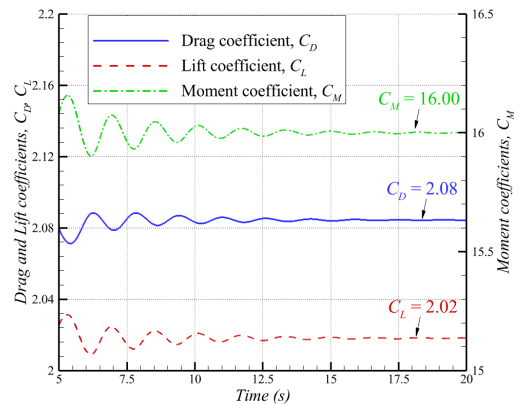

Fig. 8. Time evolution of the predicted drag, lift, and moment hydrodynamic force coefficients

Fig. 8 shows the time history of the hydrodynamic force coefficients. The numerical results exhibit a quasi-periodic variation until the time of approximately 15 (s). At the time of 20 (s), the steady stage is observed, and the corresponding drag, lift, and moment coefficients are 2.08, 2.02, and 16.00, respectively. Compared with the unbounded flow where without the presence of the free surface, the force coefficients are much larger. The measured experimental data for the unbounded flow with the Reynolds number $10^3 < Re < 10^5$ are approximate as $C_D = 1.0 - 1.2$, $C_L = 0.0$, $C_M = 0.0$. From the numerical observation, the presence of the free surface significantly affects the hydrodynamic forces on the cylinder due to the nonlinear interaction between the free surface motion and the cylinder.

3.3. Parametric investigation

In this section, the parametric investigation considering various cylinder shapes and Reynolds numbers is presented. The comparison of the circular and square cylinders is first carried out. Then, rectangular cylinders, which are characterized by the cylinder cross-section ratio defined as $AR = L/W$ (with L and W are the length and width of the cylinder, respectively), are examined. In detail, five different values of the AR ratio are adopted including 0.25, 0.5, 1.0 (square), 2.0, and 4.0. In addition, the effect of the Reynolds numbers (i.e., Re = 7,900, 11,850, and 15,800) on the hydrodynamic force coefficients are also considered. It should be noted that the water depth for all considered cases keeps the same as the validation case in Subsection 3.1.

3.3.1. *Effect of the cylinder shape on the flow field characteristics*

The free surface flow over a square cylinder shape (AR = 1.0) is first simulated with emphasis on the wake vortex formation mechanism in comparison with the circular one. All the parameters are kept the same as the validation case in Subsection 3.1. Fig. 9 shows streamline contours near the cylinder for the two cases of circular and square shapes. It
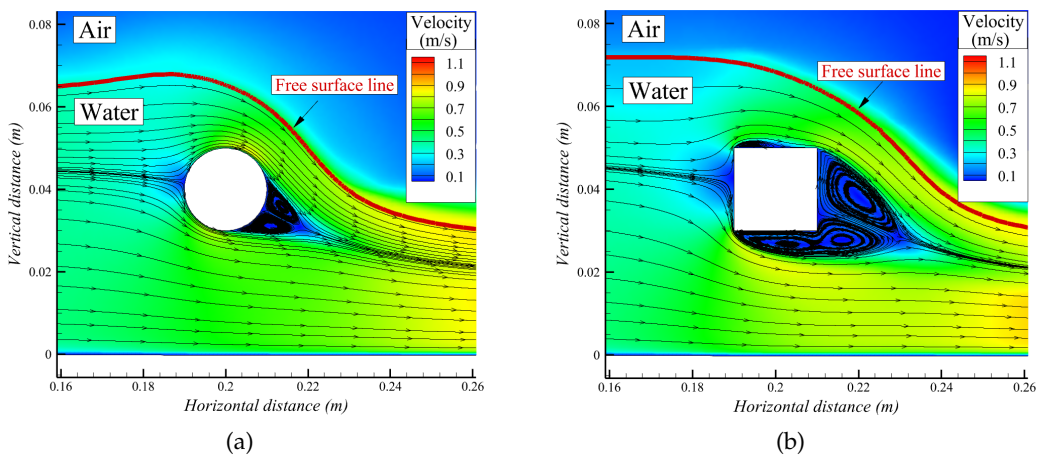

Fig. 9. Streamline contours of velocity and pressure fields for (a) circular and (b) square shapes

can be observed that a longer wake vortex behind the square cylinder, i.e., approximately two times in horizontal direction, is observed compared with the circular one. Due to the presence of the free surface, a non-asymmetric vortex in the top and bottom square surfaces is captured. Besides, two distinct vortices are observed at the bottom area, interacting with the upper vortex. The occurrence of these vortices is the main difference with the circular cylinder case. For this reason, the predicted drag coefficient significantly increases (i.e., 3.88) at the steady stage; this value is nearly two times compared with the circular case. However, the lift and moment coefficients are much smaller ($C_L = 0.2$ and $C_M = -7.61$).

3.3.2. *Effects of the shape ratio and Reynolds number on the flow field characteristics*

To further explore the flow field characteristic over rectangular cylinders, numerical simulations with five different shape ratios under three Reynolds numbers are performed. Fig. 10 shows numerical flow streamlines with the free surface for all examined cases. It is observed that the wake vortices are more significant with the decrease of AR and the increase of Re. This is because of the unstable oscillation of the free surface motion and the interaction between the upper and lower vortices and the behind one, which are more significant in the lower AR cases.
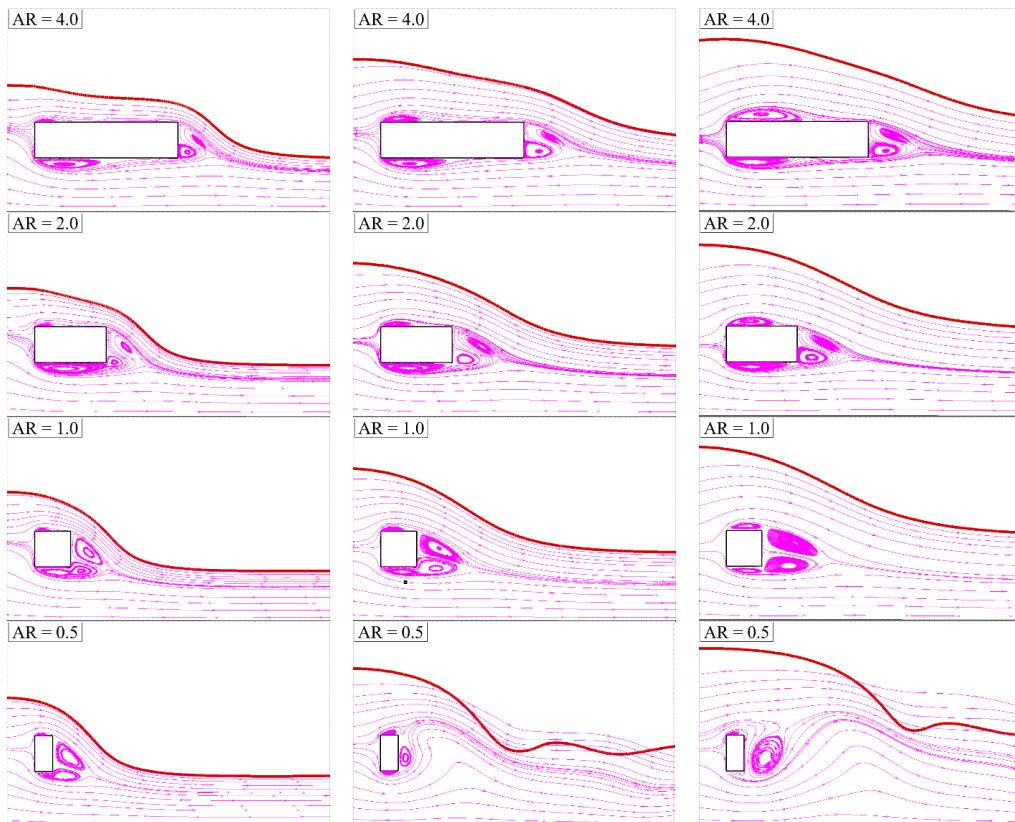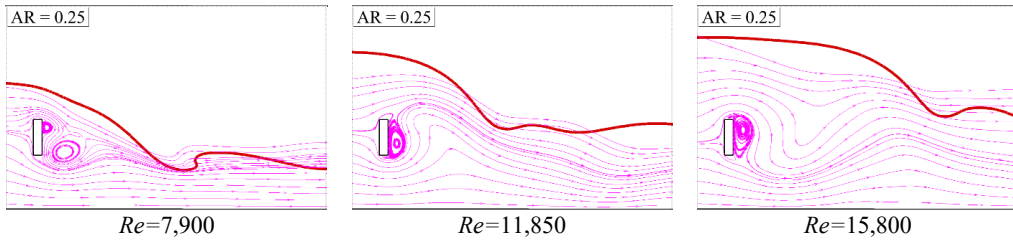
Fig. 10. Contour plots of streamlines for five different ratio shapes
under three different Reynolds numbers

For a rectangular shape of $AR = 4.0$, the upper and lower vortices are shorter than the cylinder length under three considered Re numbers, indicating that these vortices do not interact with the wave vortex on the behind. On the other side, the vortex interactions are observed in the cases of lower AR values, i.e., $AR = 2.0$, 1.0, and 0.5. For the smallest value of $AR = 0.25$, the upper and lower vortices are almost vanished, pointing out that the main vortex is behind. In addition, the water depth at the upstream section is increased with increasing of Re. The free surface shape is observed in a stable stage for larger values of $AR = 4.0$ and *2.0*. When AR decreases, the free surface is slightly fluctuated for the case of $AR = 1.0$ and becomes stronger for the cases of $AR = 0.5$ and 0.25.

3.3.3. *Effects of the shape ratio and Reynolds number on the hydrodynamic force coefficients*

The effects of the shape ratio and Reynolds number on the hydrodynamic force coefficients are presented in Fig. 11. With the increase of Re, the drag coefficient decreases for all the cases of AR whereas the lift and moment coefficients tend to increase as the AR ratio in the range of $0.5 < AR < 4.0$; this is because of the increase of the upper vortex strength together with the existing lower vortex, which both interact with the wake vortex in the behind, as shown in Fig. 10.
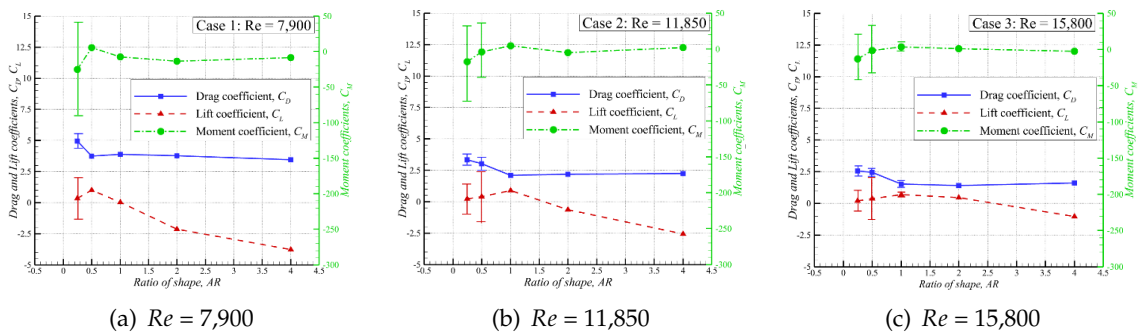

(a) *Re* = 7,900　　　　(b) *Re* = 11,850　　　　(c) *Re* = 15,800

Fig. 11. Relations of the hydrodynamic force coefficients with the shape ratio
and Reynolds number

In the case of the lowest *Re* (i.e., *Re* = 7,900), the drag coefficient remarkably decreases within *AR* = 0.25 to 0.5, and this coefficient is almost no change within *AR* = 0.5 to 4.0, as shown in Fig. 11(a). In contrast, in the first range of *AR* (*AR* = 0.25 to 0.5), the values of lift and moment coefficients are dropped. Subsequently, while the moment coefficient slightly decreases to a *AR* value of 2.0, the lift coefficient linearly decreases within *AR* = 0.5 to 4.0. Similar trends are observed for the higher *Re* numbers (see Figs. 11(a) and (b)); however, the difference is that the critical *AR* value is 1.0, i.e., the point at which the slope is significantly changed.

Besides, the force coefficients including drag, lift and moment are in a stable behavior for the cases with the larger values of *AR* under all the *Re* numbers. However, an oscillation is observed for the lower *AR* cases (*AR* $\leq$ 1.0). The amplitude of the oscillation increased with the increase of the *Re* number, which is due to the strong interaction of the vortices and free surface motions.

Fig. 12 presents the time evolution of the predicted drag, lift, and moment coefficients for the case of *AR* = 0.25 and *Re* = 7,900. It is observed that the force coefficients are in a periodic evolution feature. Fig. 13 presents the detail of the vorticity evolution around the cylinder for the case of *AR* = 0.25 and *Re* = 7,900. Eight instants cover one cycle of vortex shedding with the same time interval are plotted. The vortex structures are determined from the vorticity magnitude with values ranging from 0 to 1,000. In general, complicated vortex structures behind the cylinder with asymmetric features are observed. The main reason comes from the free surface motion above causes the overall downward movement of the vortices through pressing and pushing the up-

Fig. 12. Periodic variation of the force coefficients for the case of *AR* = 0.25 and *Re* = 7,900

per and lower shear layers, respectively. Outside the cylinder regions, vortex structures also occur in the above free surface and bottom wall boundary layers, where high gradient velocities exist. The time evolution of the free surface during one vortex shedding cycle is also measured by the red line in Fig. 13. As seen that when the lift increases from the minimum to maximum value (see Figs. 13(a)–13(e)), the free surface has rising behavior. Subsequently, the elevated free surface decreases with the lift varying from the maximum to the minimum (see Figs. 13(e)–13(h)). Besides, the interaction between the shed vorticity from the rectangular cylinder and the turbulent boundary layer developed on the channel bed is also observed. This can induce a thicker turbulent boundary layer within the interaction region and may significantly affect the hydrodynamic force coefficients.
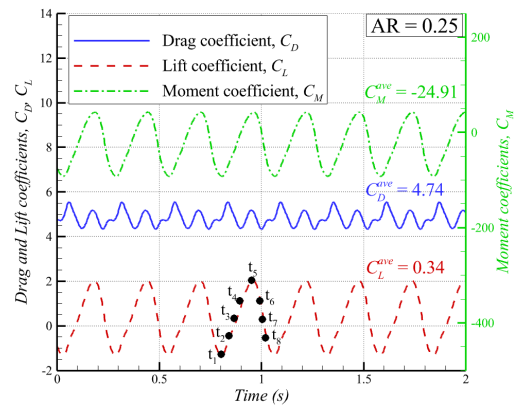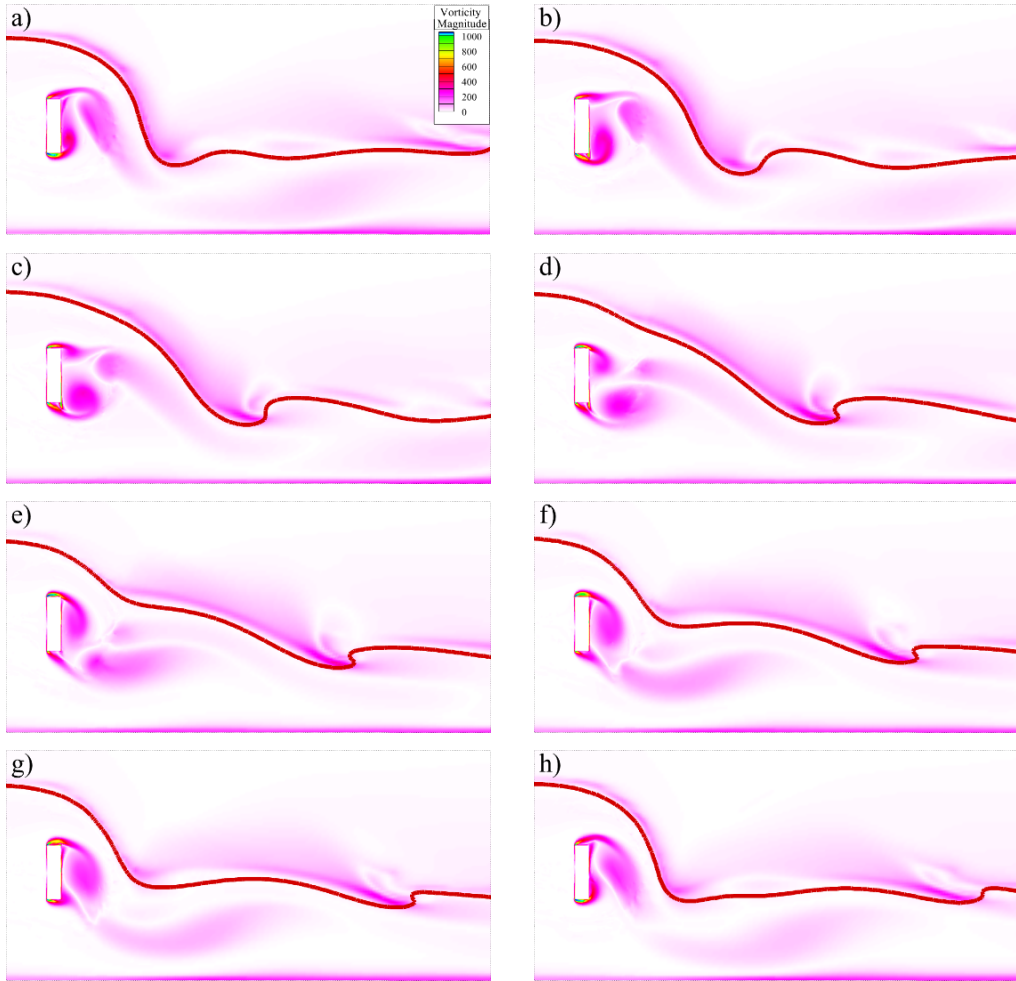
Fig. 13. Instantaneous vorticity fields around the cylinder for the case of $AR = 0.25$ and $Re = 7,900$: (a) Instant t_1 (at the minimum lift); (b) instant t_2; (c) Instant t_3; (d) Instant t_4; (e) Instant t_5 (at the maximum lift); (f) Instant t_6; (g) Instant t_7; (h) Instant t_8 (Instants t_1–t_8 indicate the stages as shown in Fig. 12)

In addition, a diagram map presenting the force coefficient behaviors under different shape ratios and Reynolds numbers is shown in Fig. 14. As shown in the figure, the decrease of AR and increase of Re promote the unstable behavior of the hydrodynamic forces. The unstable behavior exists at the lowest value of $AR = 0.25$ under the small Re number. When Re increases, this unstable behavior occurs at $AR = 0.5$ and 1.0. From $AR = 0.2$ forward, the hydrodynamic force coefficients are stable for all the cases of Re; it is recommended that this range of AR is an important criterion for the practical design of submerged civil structures under the free surface flow.
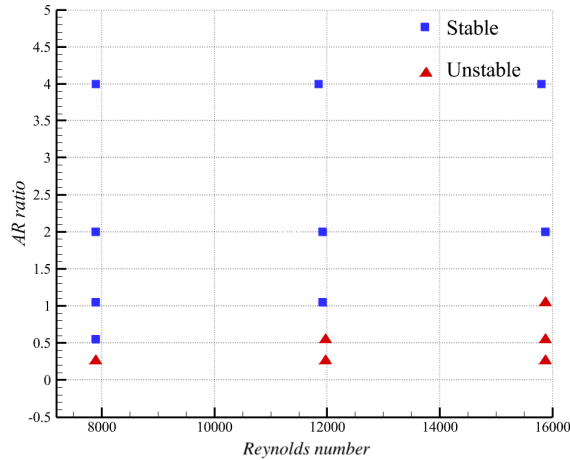
Fig. 14. Diagram of the cylinder force coefficient behavior under different shape ratios and Reynolds numbers

4. CONCLUSIONS

In the present study, nonlinear hydrodynamic forces on submerged horizontal cylinders under the free surface flow were numerically investigated. The coupling of 2D and 3D incompressible multiphase homogeneous mixture models and the VOF method was presented for computational simulations. The numerical estimation of the grid sensitivity for planar 2D and full 3D models is performed, and no obvious difference was obtained. The predicted surface pressure coefficient and free surface flow over a benchmark cylinder were compared and well-matched with the available experiment. Overall, due to the free surface effect, the cylinder wake vortex with an inclined downward direction was observed, and the numerical results also exhibited a quasi-periodic variation with reducing in the amplitude of hydrodynamic force coefficients.

In particular, the hydrodynamic forces on rectangular cylinders and free surface dynamic behavior under five different shape ratios and three Reynolds numbers were in-depth investigated using 2D simulations. It was observed that the free surface slightly fluctuates and becomes stronger with the decrease of AR and the increase of Re.

The relations of the hydrodynamic force coefficients with AR and Re values were also presented. Critical AR values of 1.0 for higher Re numbers (Re = 11,850 and Re = 15,800) and of 0.5 for the lowest Re number (Re = 7,900) were found, where the force coefficients have the opposite trend.

A diagram map presenting the force coefficient behaviors under different shape ratios and the Reynolds number was finally proposed, the hydrodynamic force coefficients were observed to be stable in a AR range of 2.0 to 4.0; this range of AR was recommended to be an important criterion for the practical design of submerged civil structures under the free surface flow.

REFERENCES

[1] J. R. Morison, J. W. Johnson, and S. A. Schaaf. The force exerted by surface waves on piles. *Journal of Petroleum Technology*, **2**, (1950), pp. 149–154. https://doi.org/10.2118/950149-g.

[2] H. N. Phan and V. L. Le. Finite volume method for prediction of wave impact loadings on vertical breakwaters and seawalls. In *the 2011 World Congress on Advances in Structural Engineering and Mechanics (ASEM11plus)*, (2011), pp. 4574–4587.

[3] M. Koken and G. Constantinescu. An investigation of the dynamics of coherent structures in a turbulent channel flow with a vertical sidewall obstruction. *Physics of Fluids*, **21**, (2009). https://doi.org/10.1063/1.3207859.

[4] G. Oliveto and W. H. Hager. Temporal evolution of clear-water pier and abutment scour. *Journal of Hydraulic Engineering*, **128**, (2002), pp. 811–820. https://doi.org/10.1061/(asce)0733-9429(2002)128:9(811).

[5] S. Malavasi and A. Guadagnini. Hydrodynamic loading on river bridges. *Journal of Hydraulic Engineering*, **129**, (2003), pp. 854–861. https://doi.org/10.1061/(asce)0733-9429(2003)129:11(854).

[6] K. Qu, W. Y. Sun, H. S. Tang, C. B. Jiang, B. Deng, and J. Chen. Numerical study on hydrodynamic load of real-world tsunami wave at highway bridge deck using a coupled modeling system. *Ocean Engineering*, **192**, (2019). https://doi.org/10.1016/j.oceaneng.2019.106486.

[7] P. Oshkai and D. Rockwell. Free surface wave interaction with a horizontal cylinder. *Journal of Fluids and Structures*, **13**, (1999), pp. 935–954. https://doi.org/10.1006/jfls.1999.0237.

[8] S. Malavasi and A. Guadagnini. Interactions between a rectangular cylinder and a free-surface flow. *Journal of Fluids and Structures*, **23**, (2007), pp. 1137–1148. https://doi.org/10.1016/j.jfluidstructs.2007.04.002.

[9] J. Bai, N. Ma, and X. Gu. Study of interaction between wave-current and the horizontal cylinder located near the free surface. *Applied Ocean Research*, **67**, (2017), pp. 44–58. https://doi.org/10.1016/j.apor.2017.06.004.

[10] C.-R. Chu, Y.-A. Lin, T.-R. Wu, and C.-Y. Wang. Hydrodynamic force of a circular cylinder close to the water surface. *Computers & Fluids*, **171**, (2018), pp. 154–165. https://doi.org/10.1016/j.compfluid.2018.05.032.

[11] H. Ren, Y. Xu, M. Zhang, S. Deng, S. Li, S. Fu, and H. Sun. Hydrodynamic forces on a partially submerged cylinder at high Reynolds number in a steady flow. *Applied Ocean Research*, **88**, (2019), pp. 160–169. https://doi.org/10.1016/j.apor.2019.04.025.

[12] P. Reichl, K. Hourigan, and M. C. Thompson. Flow past a cylinder close to a free surface. *Journal of Fluid Mechanics*, **533**, (2005). https://doi.org/10.1017/s0022112005004209.

[13] C. Bozkaya and S. Kocabiyik. Free surface wave interaction with an oscillating cylinder. *Applied Mathematics Letters*, **27**, (2014), pp. 79–84. https://doi.org/10.1016/j.aml.2013.07.009.

[14] S. Kara, T. Stoesser, T. W. Sturm, and S. Mulahasan. Flow dynamics through a submerged bridge opening with overtopping. *Journal of Hydraulic Research*, **53**, (2014), pp. 186–195. https://doi.org/10.1080/00221686.2014.967821.

[15] I.-H. Liu, J. Riglin, W. C. Schleicher, and A. Oztekin. Flow past a plate in the vicinity of a free surface. *Ocean Engineering*, **111**, (2016), pp. 323–334. https://doi.org/10.1016/j.oceaneng.2015.11.009.

[16] W. Zhong, L. Deng, and Z. Xiao. Flow past a rectangular cylinder close to a free surface. *Ocean Engineering*, **186**, (2019). https://doi.org/10.1016/j.oceaneng.2019.106118.

[17] B. Attiya, M. Altimemy, J. Caspar, C. Daskiran, I.-H. Liu, and A. Oztekin. Large eddy simulations of multiphase flows past a finite plate near a free surface. *Ocean Engineering*, **188**, (2019). https://doi.org/10.1016/j.oceaneng.2019.106342.

[18] T.-H. Phan, V.-T. Nguyen, and W.-G. Park. Numerical study on strong nonlinear interactions between spark-generated underwater explosion bubbles and a free surface. *International Journal of Heat and Mass Transfer*, **163**, (2020). https://doi.org/10.1016/j.ijheatmasstransfer.2020.120506.

[19] V.-T. Nguyen and W.-G. Park. A free surface flow solver for complex three-dimensional water impact problems based on the VOF method. *International Journal for Numerical Methods in Fluids*, **82**, (2015), pp. 3–34. https://doi.org/10.1002/fld.4203.

[20] H. N. Phan and J. Lee. Computational model for hydrodynamic pressure on radial gates during earthquakes. *Journal of the Computational Structural Engineering Institute of Korea*, **32**, (2019), pp. 323–331. https://doi.org/10.7734/coseik.2019.32.5.323.

[21] H.-N. Phan and J.-H. Lee. Flood Impact Pressure Analysis of Vertical Wall Structures using PLIC-VOF Method with Lagrangian Advection Algorithm. *Journal of the Computational Structural Engineering Institute of Korea*, **23**, (6), (2010), pp. 675–682.

[22] ANSYS Inc. *ANSYS Fluent User's Guide, 2019R1*. (2019).